
Check for updates

…ne
…ents,

…[19] and
…may cause
…nents. The
…mping gaps
…c configura-
…strap current

…urations which
…irror configura-
…otstrap currents
…n (SD, configura-
…e island geometry
…irror configuration
…erning its SOL geo-
…irror' configuration
(NHM, configuration IDs: KJM001), features a narrower toroidal mirror field and has the advantages of minimal bootstrap current compared to the standard high mirror configuration. The normalized toroidal magnetic mirror fields B_{ax}/B_0 are shown in Fig. 1 for three high mirror configurations. It is shown for various scenarios that the bootstrap current reduces with decreasing widths of B_{ax}/B_0 [21].

This study focuses on a comparison of configuration effects on the divertor heat fluxes. Namely, the standard island divertor configuration will be compared with the old and new (narrow) high mirror configurations. The conventional high mirror configuration is revisited after having been predicted to be the attractive scenario for high-performance operation from the geometric point of view (small changes of the edge topology because Shafranov shift and bootstrap currents remain small) [22]. Here, a scenario predicted by the 3D magnetohydrodynamic (MHD) equilibrium HINT code is considered to assess how the heat transport and resulting heat fluxes are affected by exemplary equilibrium effects for $\beta = 3\%$ [23].

2. 3D Modeling of plasma transport and equilibrium effects

The standard and the high mirror island divertor configurations have been implemented into EMC3-EIRENE to study the main features of plasma transport and plasma-surface interactions in current and future high-performance scenarios. EMC3-EIRENE is a fully 3D coupled plasma fluid and kinetic edge transport Monte Carlo code. EMC3 solves a set of reduced Braginskii fluid equations for particles, parallel momentum, and energies for electrons and ions [24,25]. EIRENE solves the kinetic transport equations for neutral atoms and molecules including

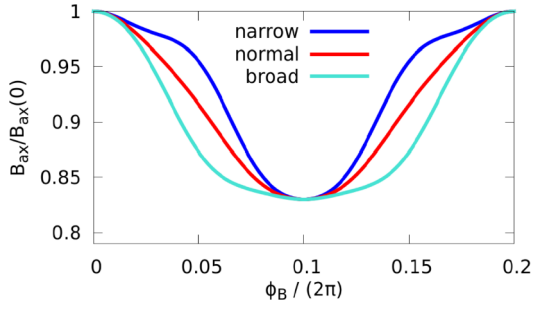

Fig. 1. Toroidal magnetic mirror field for Narrow High Mirror (NHM, blue), High Mirror (HM, red) and Broad Mirror (cyan). (For interpretation of the references to colour in this figure legend, the reader is referred to the web version of this article.)

…classi…
…source/loss …
…ionization, are calculated …
…eled based on a fluid approach within EMC3 …
the main plasma by excitation and ionization. The perpendicular transport is determined by coefficients for anomalous particle transport $D_\perp$ and anomalous electron and ion heat transport $\chi_{\perp,\,e,\,i}$ which are free model parameters. The electron and ion heating power are defined at the inner simulation boundary, and the upstream density is set near the separatrix. HINT is a 3D MHD equilibrium calculation code which does not assume nested flux surfaces [27]. It uses a relaxation method based on the dynamic equations of the magnetic field and pressure. The first step consists of a relaxation process of the plasma pressure satisfying the condition $\boldsymbol{B}\cdot\nabla p = 0$ for a fixed $\boldsymbol{B}$. The second step is a relaxation process of the magnetic field for a fixed p, where an equation of motion (neglecting the non-linear convective term) and the induction law are solved towards steady state. The final equilibrium state corresponds almost to a stable steady-state satisfying force balance. One high-performance scenario based on a HINT calculation is implemented and discussed in this study.

Transport simulations have been performed for upstream densities $n_{up} = 0.5 - 2{\cdot}10^{19}$ m^{-3} and input powers between 3.0 MW and 8.0 MW in this study. Carbon is assumed as the main impurity responsible for total radiative power losses of P_{rad}= 0.5 MW. Values of $\chi_{\perp,i,e} = D_\perp$=0.5 m^2 s^{-1} are typically used as anomalous transport coefficients for heat and particles based on W7-AS experience [28]. These results are compared with dedicated experiments while the equilibrium case anticipates plasma response effects in future higher performance scenarios.

3. Geometric properties of the island divertor

The scenarios considered in this study were conducted in ι=5/5 island divertor configurations [14]. This means that five independent helical island bands establish the equivalent of the SOL in tokamaks and hence render the extension of the core confinement domain. Ten graphite divertor units represent the main plasma facing components.

The target-to-target connection lengths L_C have been calculated for the island divertor configurations considered to evaluate the geometry effects relevant for the plasma transport and the plasma surface interactions. Three configurations extended by one higher pressure scenario are assessed in this study. The L_C profiles of the experimentally realized standard divertor configuration, the (new) narrow high mirror configuration and the (old) high mirror are shown in Fig. 2(a–c) at a toroidal cross section $\Delta\phi = 12.3°$ distant from the bean-shaped symmetry cross-section. Poincaré plots of the vacuum field are superimposed (black dots). The connection lengths are of O(100 m) within the islands (blue, purple, red domains) and may obey lengths of O(1 km) (yellow) at the separatrix. The outermost layer consists of short L_C of O(1–10 m).

The connection length calculations reveal that the island SOL geometry of SD and NHM are very similar at first glance (Fig. 2(a) and (b)). Both show separatrix legs connecting to the horizontal and vertical divertor target plates (shown as solid red lines) almost at the same locations. The interior of the islands consists of $L_C \approx$ 300 m. In case of SD and NHM, parts of the island O-points are present as small sub confinement domains not intersected by target plates. In the old high mirror configuration the islands are cut deeper featuring no closed field lines around the island O-points (Fig. 2(c)). There is stronger shadowing effect by the vertical targets. These results show, that the large degree of freedom in configuration space allows for an optimization of both, core transport (high mirror and low bootstrap currents) and edge magnetic topology with respect to a target deposition pattern.

The impact of changes of the magnetic SOL topology on the divertor heat fluxes will be discussed in the following. It will be demonstrated

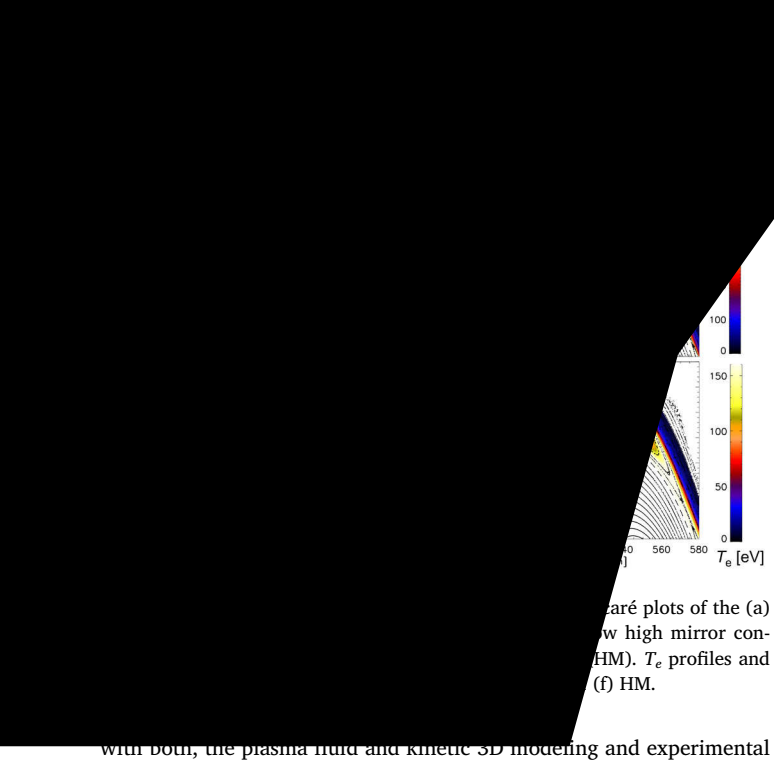

…aré plots of the (a) …w high mirror con- …HM). T_e profiles and (f) HM.

with both, the plasma fluid and kinetic 3D modeling and experimental measurements the configuration optimization can strongly modify, even reverse major features of the divertor heat flux distributions even within 5/5 configurations. Adding equilibrium effects may result in more significant changes with respect to the vacuum approximations.

4. Impact of island topology on divertor heat fluxes

The three configurations of interest are compared concerning the impact of their edge magnetic topology on the divertor heat load

operat…

During thi…

lower performance. A lot …

commissioning. Dedicated experiments were …

line integrated densities measurements (interferometer), bolometer measurements or some SOL measurements with the Helium beam in order to constrain the modeling.

The IR cameras are the most suitable diagnostics providing heat fluxes deposited on most of the divertor modules [29]. Their almost complete toroidal coverage allows for the best local and global comparison between the modeled and measured heat flux distributions.

Typical scenarios with electron-cyclotron-resonance heating (ECRH) of 3 MW are considered and $\int n_e dl \approx 2 \cdot 10^{19}$ m^{-2}. A SOL electron and density profile measurement based on state of the art collisional-radiative modeling [30] is shown in Fig. 4(a,b) for the SD scenario analysed in the following. It shows typically SOL temperatures of $T_e \approx 50 - 100$ eV and densities in the range of $n_e \approx 0.2 - 0.5 \cdot 10^{19}$ m^{-3}. The radiated power was estimated from Bolometer measurements available and varies for these plasma conditions typically between $P_{rad} = 0.5 - 1.0$ MW.

The results from 3D modeling show a strong impact of the island SOL geometry on heat and particle transport. The electron temperature distribution in the island divertor volume in Fig. 2(d–f). The comparison with the L_C in Fig. 2(a–c) shows a clear pattern in the heat transport induced by the island geometry. The hottest parts are found in the flux tubes around the separatrix while the island center remains cold. The reason is that the long flux tubes within and close to the separatrix receive most of the heat and particles diffusing out of the hot confinement. The fast parallel convective and conductive heat transport

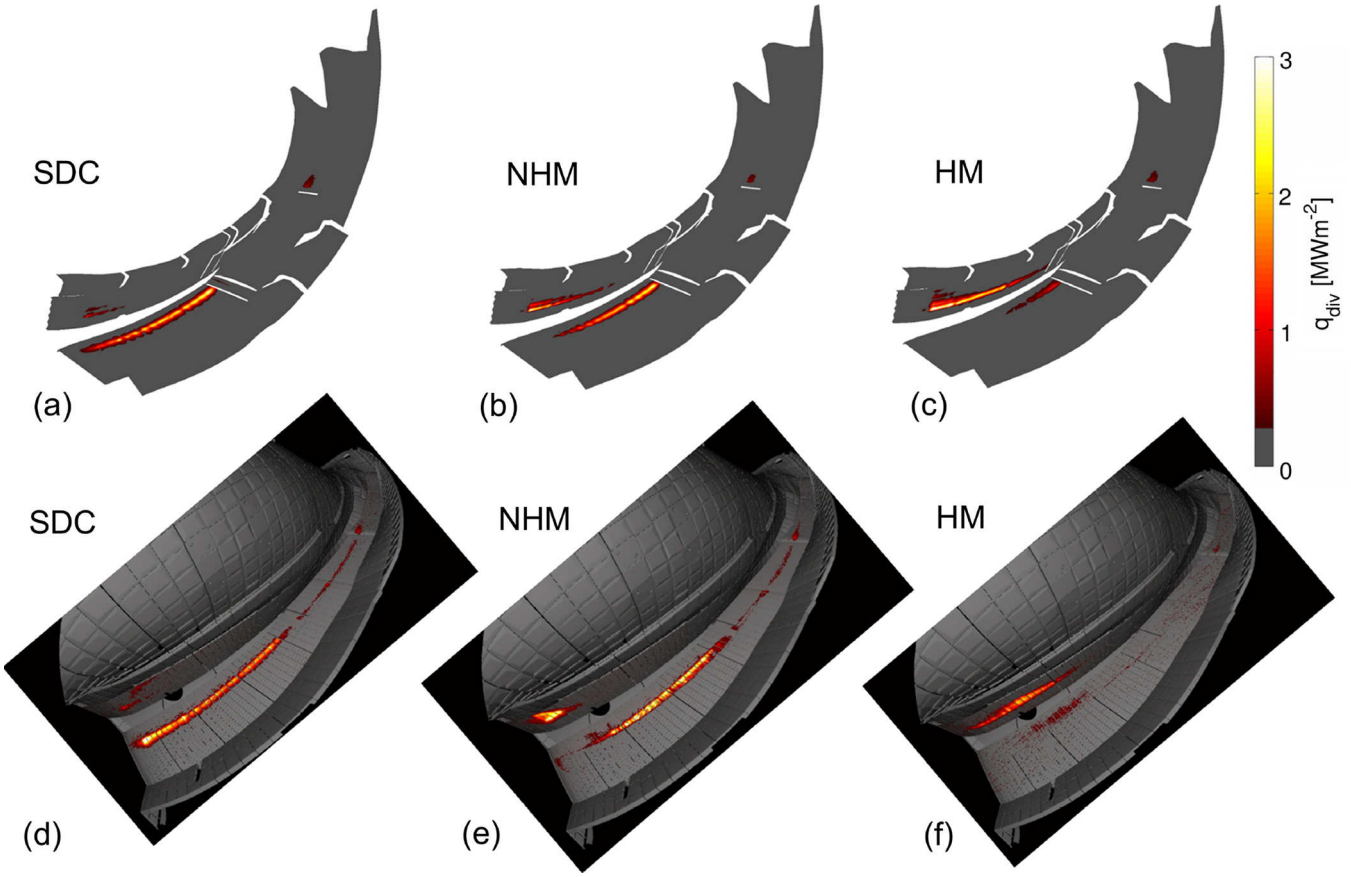

Fig. 3. Comparison of modeled divertor heat fluxes (a–c) and heat fluxes from IR measurements for (d–f) for standard divertor, narrow high mirror and high mirror configuration.

et [cm]

with the He

dly on the hor-
aratrix legs are
following the L_C
a, b)). In the HM
om the horizontal
arget in correlation
L_C profile (compare
ng recovered in the
heat flux mapping.

A comparison of modeled and measured divertor heat fluxes onto the divertors q_{div} is shown in Fig. 3(a–f) for the same heat flux scale. The experimental data shown (d–f) correspond to the heat fluxes on a top divertor (module 5, AEF51) at $t - t_1 \approx 0.99$ s and are taken from the experiments #20171114.052 (SD), #20170926.071 (NHM) and #20171122.033 (HM).

The main heat stripes or strike lines occur where the long open field lines of the separatrix connect to the divertor targets (compare with L_C vs. T_e Fig. 2(a–f)). The modeling predicts that the main fraction of integrated heat fluxes are deposited on the horizontal target in the SD (a) while the loads are distributed more evenly between the horizontal and vertical target in the NHM configuration (b). For the HM configuration, the heat fluxes are mostly directed onto the vertical target (c). These predictions are qualitatively in good agreement with the measured heat fluxes depicted in Fig. 3(d–f).

The heat flux profiles across the divertor targets have been averaged over the main wetted area in the toroidal direction in both modeling and experiment and are shown in Fig. 5(a–c). The comparison reveals a significant scattering of the experimental profile data (squares). In the SD configuration, the average peak maxima vary between 0.5 and 2.25 MWm^{-2} depending on the divertor considered. Moreover, the peak maxima positions have relative offsets of up to 5 cm with respect to

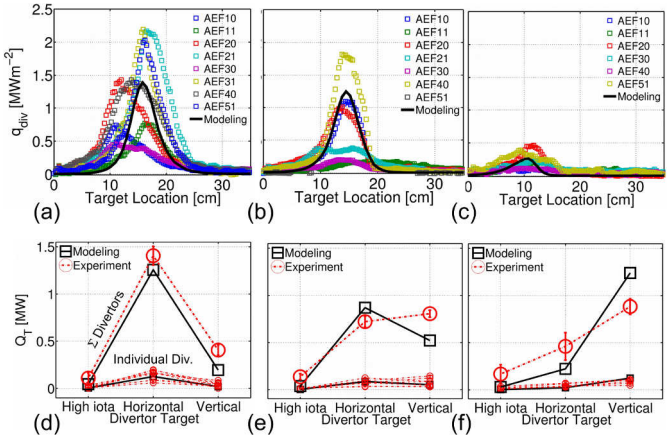

Fig. 5. Top: comparison of modeled (solid line) and measured (squares) averaged divertor heat flux profiles across the horizontal target for (a) the standard, (b) the narrow high mirror and (c) the high mirror configuration. Bottom: (d–f) comparison of individual and total heat loads onto the main wetted divertor targets (high iota, horizontal and vertical target).

below
may first of
ditional asymmetries, but
is a matter of ongoing development. A first
heat flux data and analysis of the scaling behaviour will be reported elsewhere.

The measurements confirm the main features predicted by modeling. The heat load is centered around the separatrix. The shape of the heat flux profile is in particular determined by the competition of parallel and perpendicular transport in the divertor volume. A convolution of an exponential profile with a Gaussian function according to the heuristic drift-based model [32] may not hold anymore in the complex 3D geometry introduced above.

Consider the total distribution on the three main wetted divertor parts in Fig. 5(d–f). The small red circles represent the loads on individual divertors at $t - t_1 = 0.99$ s. The big red circles represent the total loads onto the respective components. The black squares represent the loads obtained from 3D modeling assuming the same upstream and heating conditions for all configurations. The high iota part of the divertor receives the smallest load (but still more than the remaining components not depicted). The horizontal target receives most load in the SD (3.5 times more than the vertical target). The NHM configuration shows experimentally an almost equal distribution between horizontal and vertical target compared to the modeling which instead predicts a reversed ratio with most loads on the horizontal target. The vertical target receives most heat load in the high mirror configuration (2 times more than the horizontal target).

Uncertainty analysis within the modeling was mostly done based on density scans showing that in SD the ratio between loads onto horizontal and onto vertical target may reduce from 3.5 to 2 for densities increased from $2 - 8 \cdot 10^{19}$ m^{-3} while this ratio varies between 1.1 and 1.3 in the NHM configuration. However, this scattering is marginal compared to the scattering observed experimentally. The magnetic fields of these initial low-performance plasmas can be sufficiently approximated based on vacuum fields. Deviations in the edge magnetic structure are mostly suspected to be due to error fields. The potential impact of equilibrium effects in high-performance scenarios is discussed in the following.

5. Predicted impact of equilibrium effects

The high mirror configuration was considered to be favorable due to the reduced bootstrap currents potentially degenerating the regular island geometry. Therefore, a first prediction is made for a high mirror equilibrium scenario assuming $\beta = 3\%$ obtained from the 3D MHD code HINT [23]. Significant equilibrium changes are due to the build-up of a substantial plasma pressure which causes a Shafranov shift.

The effects on the island geometry are shown in the L_C profile and superimposed Poincaré plots in Fig. 6(a) for the main island divertor volume $\Delta\phi = 12.3°$ distant from the bean-shaped symmetry cross-section. The magnetic field of the high mirror equilibrium scenario in Fig. 6(a) shows an enhanced stochastization of the boundary magnetic field, in particular of the island separatrix. These are major changes compared to the vacuum topology of this configuration (Fig. 2(c)). The open field line domain features patterns with poloidal modulation of L_C within the islands. The geometrical effects most relevant for plasma edge transport and plasma surface interactions are increased island sizes and reduced L_C, which means a change of the path lengths for perpendicular and parallel transport.

The separatrix legs in the equilibrium case are shifted compared to their locations in the vacuum case. As a result, the top right separatrix leg connects to the horizontal divertor plate in this cross-section.

The plasma edge transport has been calculated with EMC3-EIRENE assuming upstream densities $n_{up} \approx 6 \cdot 10^{19}$ m^{-3} and $P = 10$ MW for both

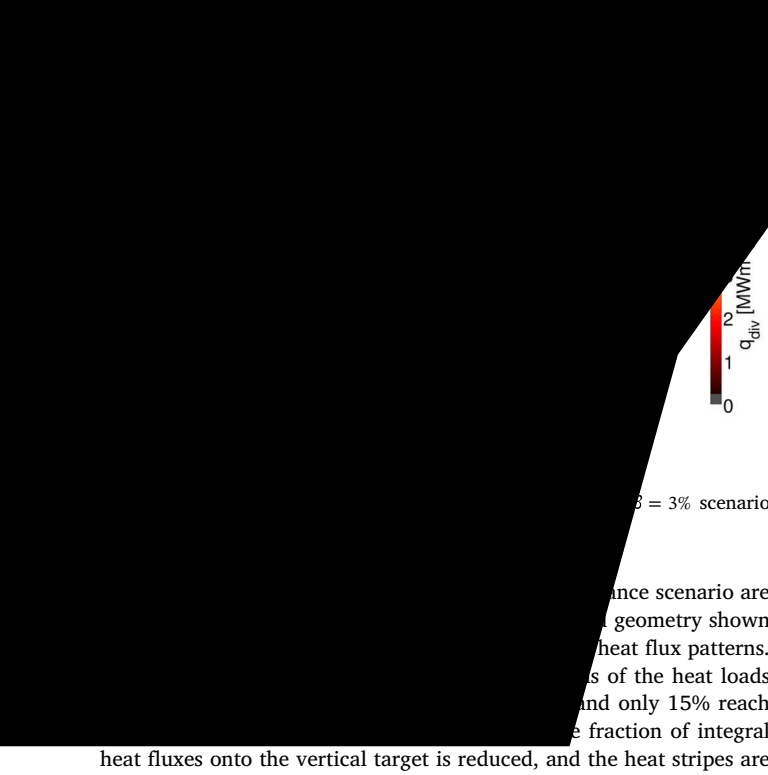

= 3% scenario

nce scenario are
geometry shown
heat flux patterns.
s of the heat loads
nd only 15% reach
fraction of integral
heat fluxes onto the vertical target is reduced, and the heat stripes are more narrow. Heat stripes close to the pumping gap might become a concern due to overloading of more sensitive components. Also, a second primary heat stripe occurs on the opposite side of the horizontal target remote from the pumping gap. The fraction of heat fluxes onto the vertical target reduces to 50% while total fractions from both heat stripes onto the horizontal plate account for 30–35%.

The heat fluxes onto the divertors turn out to reduce in widths despite to the fixed anomalous cross field coefficients. In this case, the change of heat fluxes is purely induced by the geometry. The responsible parameter narrowing the main heat flux channels around the island separatrices are the parallel transport lengths: $< L_C >_{\beta=3\%} \approx 0.5 < L_C >_{vac.}$.

In a simplified SOL flux tube picture the parallel energy transport is enhanced according to $\tau_{E\parallel} \propto \frac{L_C}{V_\parallel}$ reducing the heat flux channel widths according to $\lambda_{q\parallel} \propto \sqrt{L_C}$ [33].

This first implementation of HINT into EMC3-EIRENE shows that the equilibrium response may induce changes to the island divertor geometry resulting into strong redistributions of divertor heat fluxes. At the same time, a significant fraction of the recycling is redirected away from the pump location which may affect the exhaust of neutrals. Once accessible, such scenarios will also be implemented into EMC3-EIRENE based on 3D equilibrium reconstruction with V3FIT [34,35].

6. Conclusions

An analysis of the effects of the 3D island geometry of standard divertor and high mirror configurations on the heat load distributions has been performed based on 3D modeling and IR data. The new narrow high mirror configuration has been implemented and investigated for the first time to demonstrate the success of its core-edge optimization.

The global analysis of the load distribution shows a good qualitative agreement between measurement and modeling and confirm the role of the island geometry for the divertor heat flux patterns. The island separatrix is the main heat flux channel, and its position determines the position of the strike lines on the divertor targets.

The change of island geometry between the configurations leads to a substantial re-distribution of heat loads between the main wetted targets. The narrow high mirror configuration is confirmed to feature a more even heat load distribution on horizontal and vertical divertor target. This may be desired to spread the heat loads and allows for better characterization of the plasma-surface interactions with diagnostics optimized for the standard configuration.

toroid
experimental p
significant differences in
further investigated, a strategy to allow
between experiment and 3D modeling in case of given asymmetries is under development.

Extrapolation towards high-performance scenarios was done for the first time based on an implementation of 3D MHD HINT equilibrium calculations for $\beta = 3\%$ with EMC3-EIRENE. The analysis of the SOL geometry shows an increase of the island sizes, a shift of the separatrix legs and a decrease of L_C resulting in narrower heat flux channel widths and redistribution of the heat fluxes.

The local deviations between modeled and measured heat fluxes and moreover the 3D MHD effects predicted for higher performance scenarios will motivate a coupling of EMC3-EIRENE to 3D equilibrium reconstruction once developed.

Acknowledgements

This work was supported in part by the U.S. Department of Energy (DoE) under grant DE-SC0014210 and by discretional funding of the Department of Engineering Physics and the College of Nuclear Engineering at the University of Wisconsin - Madison, USA. The publisher, by accepting the article for publication acknowledges, that the United States Government retains a non-exclusive, paid-up, irrevocable, worldwide license to publish or reproduce the published form of this manuscript, or allow others to do so, for United States Government purposes. This work has been carried out within the framework of the EUROfusion Consortium and has received funding from the Euratom research and training programme 2014–2018 and 2019–2020 under grant agreement No 633053. The views and opinions expressed herein do not necessarily reflect those of the European Commission. This work is partially supported by the Japan Society for the Promotion of Science Grant-in-aid for Scientific Research (B) 18H01202. This research was performed using the computer resources and assistance of the UW-Madison Center For High Throughput Computing (CHTC) and the high-performance computing system DRACO of the Max-Planck-Gesellschaft at Rechenzentrum Garching (RZG).

References

[1] M. Kobayashi, et al., Nucl. Fusion 55 (2015) 104021.
[2] R. König, et al., Plasma Phys. Controlled Fusion 44 (2002) 2365.
[3] M. Kobayashi, et al., Nucl. Fusion 53 (2013) 033011.
[4] S. Dai, et al., Plasma Phys. Controlled Fusion 59 (2017) 085013.
[5] Y. Feng, et al., Contrib. Plasma Phys. 44 (2004) 57.
[6] Y. Feng, et al., Nucl. Fusion 46 (2006) 807.
[7] A. Bader, et al., Nucl. Fusion 53 (2013) 113036.
[8] A.R. Akerson, et al., Plasma Phys. Controlled Fusion 58 (2016) 084002.
[9] S. Marcinko, D. Curreli, Phys Plasmas 25 (2018) 022507.
[10] J. Nührenberg, et al., Fusion Technol. 27 (1995) 71.
[11] R.C. Wolf, W.-X. Team, Contrib. Plasma Phys. 49 (2009) 671.
[12] S. Bozhenkov, et al., Limiter for the early operation phase of W7-X, 41st EPS Conference on Plasma Physics, 38F Europhysics Conference Abstracts (ECA), Berlin, 2014.
[13] T.S. Pedersen, et al., Nucl. Fusion 55 (2015) 126001.
[14] T. Andreeva, et al., Prob. At. Sci. Technol. Ser. 4 (2002).
[15] A. Dinklage, et al., Nat. Phys. 14 (2018) 855.
[16] F. Effenberg, et al., Nucl. Fusion 57 (2017) 036021.
[17] G. Wurden, et al., Nucl. Fusion 57 (2017) 056036.
[18] J. Geiger, et al., Contrib. Plasma Phys. (2010) 50770 https://doi.org/10.1002/ctpp.200900028.
[19] J. Geiger, et al., Plasma Phys. Controlled Fusion 57 (2015) 014004.
[20] H. Hölbe, et al., Nucl. Fusion 56 (2016) 026015.
[21] J. Geiger, et al. Plasma equilibrium and core confinement on W7-X with an island divertor, 2017.
[22] Y. Feng, et al., Nucl. Fusion 56 (2016) 126011.
[23] Y. Suzuki, J. Geiger, Plasma Phys. Controlled Fusion 58 (2016) 064004.
[24] Y. Feng, et al., Contrib. Plasma Phys. 44 (2004) 57.
[25] Y. Feng, et al., Contrib. Plasma Phys. 54 (2014) 426.

[34] J.D.
[35] J. Schmitt, et